Science Advances

AAAS

advances.sciencemag.org/cgi/content/full/3/4/e1602564/DC1

Supplementary Materials for

SAVI: Synthetic apertures for long-range, subdiffraction-limited visible imaging using Fourier ptychography

Jason Holloway, Yicheng Wu, Manoj K. Sharma, Oliver Cossairt, Ashok Veeraraghavan

Published 14 April 2017, *Sci. Adv.* **3**, e1602564 (2017)
DOI: 10.1126/sciadv.1602564

This PDF file includes:

Supplementary Materials

A. Limitation for a Lens with a Large Aperture

For a fixed focal length, spatial resolution in long distance imaging is fundamentally limited by diffraction blur and turbulence. In this paper we restrict our analysis to the effect of diffraction blur and do not consider turbulence. Diffraction blur is governed by the diameter of the camera's aperture—using a lens with a larger aperture will lead to increased spatial resolution. However, physically increasing the aperture of the lens is not an ideal solution. Figure S1 illustrates the rapid increase in cost and weight of commercial lenses as the focal length increases. The cost and weight are a consequence of increasing lens diameter, as well as the plethora of corrective optics required to counteract aberrations in these larger lenses. A system designer is faced with a difficult choice: use a long focal length and pay for an enormous lens, or use a shorter focal length and sacrifice spatial resolution.

B. Related Methods for High-Resolution Imaging

Improving spatial resolution in coherent imaging systems has a rich history that predates the widespread adoption of digital image sensors. The coherent fields of interest in imaging applications are complex-valued 2D functions that map propagating light to a set of electric field amplitude $A(x, y)$ and phase $\theta(x, y)$ values

$$U(x, y) = A(x, y)e^{j\theta(x,y)} \tag{1}$$

where j is the imaginary unit. In contrast to incoherent imaging, this complex phasor representation encompasses the effects of interference and diffraction. One consequence of using coherent illumination is the formation of speckles if the wave passes through an inhomogenous medium or reflects off a diffusive surface.

Refractive telescopes: (*1*, *4*–*6*) Speckle reduction and super-resolution is of particular interest for terrestrial astronomy. Spatially coherent light from distant stars encounters turbulence upon entering Earth's atmosphere which manifests as speckle at the imaging plane. It was observed by Fried (*1*) that averaging multiple short exposure images produced a composite image with better resolution than a single image captured with a long exposure. Korff (*2*) proved that summing short-exposure intensity images, retains high frequency information that is lost in long exposure recordings, while Miller et al. (*3*) showed that averaging images results in the incoherent observation. Knox and Thompson (*4*) proposed using just two offset speckle images to estimate the amplitude and phase of the diffraction limited image. Further refinements such as using adaptive optics to correct for turbulence eliminate the need to capture multiple measurements and enable longer exposure times to increase signal strength (*5*, *6*). While the proposed methods successfully reduce speckle, the resolution is still limited to diffraction blur imposed by the lens' diameter.

Holography: Since its discovery in 1948 by Gabor (*53*), holography has been a powerful tool for capturing the complex light field of a scene. The full complex field is interferometrically recorded,

preserving full spatial resolution of a scene. Unlike traditional photography, holography requires special care during data capture (to prevent motion and to limit ambient light contamination) and a custom viewing platform. In microscopy, where all variables can be carefully controlled, holography is a powerful tool (*54*).

Holographic systems measure the phase of the complex field incident on the detector, permitting a relatively straightforward implementation of synthetic aperture imaging. Holography has been extended to create synthetic apertures in microscopy (*7*) and on-axis holography (*8*) Of particular interest are off-axis techniques which are more applicable to long-distance imaging. Early efforts to create synthetic apertures in an off-axis geometry found moderate success, resolution was improved by 2.5−3× at a working distance of less than one meter (*9*, *10*). Tippie et al. (*11*) demonstrated an off-axis holographic method to get a high-resolution image with 9.5× improvement.

Incoherent super-resolution (see fig. S2 for comparison with SAVI): The techniques used in this paper rely on coherent illumination to image beyond the diffraction limit of the lens. Using incoherent illumination would improve resolution and remove speckle in individual captured images, but it also precludes creating a synthetic aperture. Multi-image super-resolution methods for incoherent measurements offer only a 2× resolution improvement (*12–14*). Dictionary-based reconstructions improve resolution by approximately 4×, but cannot guarantee image fidelity (*15*, *16*). Moreover, incoherent super-resolution does not account for diffraction limited imaging systems, and the performance of multi-image super-resolution algorithms suffers.

Holloway et al. (*32*) compare the efficacy of using multi-image incoherent super-resolution and FP for diffraction limited systems, but only consider optically smooth objects. Here we extend comparison to incorporate random phase and conclude that coherent illumination and SAVI are still better suited for creating affordable long-distance imaging systems. Three common multi-image super-resolution techniques are used to reconstruction a high-resolution image: Papoulis-Gerchberg super-resolution (*38*, *55*), robust super-resolution (*56*), and normalized convolution (*57*). All three incoherent algorithms are implemented using code from (*58*).

In fig. S2, we simulate super-resolution for both incoherent and coherent illumination using a lens with large diameter and a lens with significantly smaller diameter. A high-resolution object (536 × 536 pixels, shown in full in Fig. 6) is imaged onto a 67×67 pixel sensor resulting in an 8× loss in resolution. The pixel pitch of the sensor is set to be 1.8 μm. In fig. S2(A), a lens with a large aperture (f/5.6) produces a diffraction spot size of 3.7 μm, or 2 pixels. As expected, the incoherent observation is free of speckle, however each of the four image super-resolution techniques only show a modest improvement in spatial resolution. Coherent imaging results in speckle, but thanks to the larger synthetic aperture, finer features are observed.

Achieving the relatively small diffraction in fig. S2(A) requires using a lens with a large diameter, a potentially costly prospect. If a lens with a significantly smaller aperture (f/32) were to be used instead, the diffraction spot size would increase to 20.7 μm, or about 11.5 pixels. In the large blur regime, incoherent image super-resolution techniques are unable to improve image resolution. SAVI, on the other hand, is able to improve image resolution and surpass the image quality of the incoherent measurements.

The limited ability to increase spatial resolution suggests that incoherent illumination cannot outperform coherent imaging for long-distance super-resolution.

Fourier Ptychography: Fourier ptychography is an alternative method creating a synthetic aperture by sampling a diverse set of regions in Fourier space. Unlike holography, FP does not require the use of a reference beam to encode phase information. The phase of the complex field is recovered computationally in post-processing. FP has found much of its success in microscopy. Early efforts by Kirkland et al. (*59*, *60*) demonstrated that multiple images recorded with different incident beam tilts could be used to effectively double image resolution. Zheng et al. (*17*) provided a complete framework for FP microscopy and demonstrated wide-field, high-resolution imaging. Subsequent research has improved the quality of FP reconstructions by characterizing the pupil function (*18*), digitally removing optical aberrations (*19*), and refocusing the recovered image postcapture (*20*). FP microscopy (where the illumination direction is varied) inherently assumes that the sample may be modeled as a thin object. Extensions for thick biological samples (*21–23*) have been proposed at the expense of increased computational complexity.

Dong et al. (*24*) and Tian et al. (*25*) independently demonstrated that mutually-incoherent sources could be multiplexed to drastically reduce acquisition time and increase signal strength. Sparse measurement masks can also be used to reduce the amount of data needed at each illumination position (*26*). Acquisition time can also be reduced by leveraging the weakly scattering nature of biological samples to undersample portions of the Fourier domain (*27*).

Phase retrieval: At the heart of FP is the requirement to recover the phase of the light field at the aperture plane of the lens, which subsequently provides knowledge of the field at the object plane. Phase retrieval is also an important step in standard ptychography and many of the techniques used in FP are borrowed from these earlier efforts.

In general, closed form solutions for recovering phase information require prohibitively large datasets to be practical (*61–63*). Iterative solutions are thus preferred for ptychographic reconstruction. Many FP

reconstruction algorithms are based on the iterative update schemes first proposed by Gerchberg and Saxton (*28*) and Fienup (*29*). Maiden and Rodenburg (*30*) introduced the ePIE technique to jointly estimate the field at the detector and the probe used for illumination. Ou et al. (*18*) adapted ePIE for use in FP whereby the pupil function is jointly estimated with the field at the aperture plane. Experimental robustness of various phase retrieval algorithms were characterized by Yeh et al. (*31*) who conclude that minimizing the error in amplitude and using second-order gradient descent methods provide the best results. The phase retrieval algorithm used by Tian et al. (*25*), which incorporates the pupil update step of (*18*) and uses the second-order Newton's method as the numerical solver, serves as the base of our proposed algorithm. Although the objective function of the reconstruction framework in (*25*) minimizes intensities and not amplitudes, we observe good reconstruction quality in our experiments.

C. Forward Model Using a Focusing Lens

The forward model described in Section II assumes that the separation distance between the object and camera lens satisfies the Fraunhofer approximation for far-field diffraction. Far-field approximations are valid when the distance between the object and camera is greater than (*37*)

$$z > \frac{2d^2}{\lambda} \tag{2}$$

For the experimental setup described in this paper (λ = .532 μm, d = 2.5 mm), the camera would have to be positioned at least 25 meters away from the target for Eq. (2) to hold. Increasing the aperture ten-fold would require a separation distance of at least 2500 meters.

To circumvent the massive separation requirements necessary to satisfy the Fraunhofer approximation organically, a lens is used to focus light on the aperture of the camera, which also satisfies the Fraunhofer approximation. Here we demonstrate that the analysis presented in Section II holds for our experimental setup and that use of a focusing lens incurs no additional penalty beyond an extra quadratic phase term. A more rigorous formulation of the forward model is demonstrated using Fresnel propagation.

For compactness, the analysis in this section follows the operator notation presented in (*37*). Free-space propagation is denoted by R[a], scaling by a constant is denoted by V[b], and multiplication by a quadratic-phase exponential is denoted by Q[c]. These three terms are defined as operating on field $U(\mathbf{x})$ as

$$\mathcal{R}[a]\{U(\mathbf{x_1})\} = \frac{1}{\sqrt{j\lambda a}}\int_{-\infty}^{\infty} U(\mathbf{x_1}) e^{j(k/2a)(\mathbf{x_2}-\mathbf{x_1})^2}\,\mathrm{d}x_1$$

$$\mathcal{V}[b]\{U(\mathbf{x})\} = \sqrt{|b|}\,U(b\mathbf{x})$$

$$\mathcal{Q}[c]\{U(\mathbf{x})\} = e^{j\frac{k}{2}c\mathbf{x}^2} U(\mathbf{x})$$

The Fourier transform is denoted by the operator $\mathcal{F}$.

A simplified illustration of the imaging configuration is shown in fig. S3, where the distances between each optical element are labeled. Note that in the experiment, the coherent source is passed through a pinhole which is approximated as the point source shown in fig. S3. In the experiment two constraints on the geometric optics are satisfied though the well-known lens law

$$\frac{1}{z_1}+\frac{1}{z_2+z_3}=\frac{1}{f_1} \tag{3}$$

$$\frac{1}{z_3}+\frac{1}{z_4}=\frac{1}{f_2} \tag{4}$$

Let the complex reflectivity function of the object be denoted as $\mathcal{O}$. Analysis of this system is separated into three stages, propagation from the light source to the object plane, propagation from the object to the aperture of f_2, and finally propagation from the aperture to the image sensor plane. These three stages are denoted as S_1, S_2, and S_3 respectively.

Spherical waves emanating from the laser source are modeled as a quadratic-phase exponential. Light from the source travels a distance z_1 to the focusing lens ($\mathcal{Q}$ [$1/z_1$]), picks up a quadratic phase from the lens ($\mathcal{Q}$ [$-1/f_1$]), and propagates a distance z_2 ($\mathcal{R}$ [z_2]) to the object. The field immediately after the object is

$$\begin{aligned}
\mathcal{O}S_1 &= \mathcal{O}\mathcal{R}[z_2]\mathcal{Q}\left[-\frac{1}{f_1}\right]\mathcal{Q}\left[\frac{1}{z_1}\right] \\
&= \mathcal{O}\mathcal{R}[z_2]\mathcal{Q}\left[-\frac{1}{f_1}\right]\mathcal{Q}\left[\frac{1}{f_1}-\frac{1}{z_2+z_3}\right] \\
&= \mathcal{O}\mathcal{R}[z_2]\mathcal{Q}\left[-\frac{1}{z_2+z_3}\right] \\
&= \mathcal{O}\mathcal{Q}\left[-\frac{1}{z_3}\right]\mathcal{V}\left[\frac{z_2+z_3}{z_3}\right]\mathcal{R}\left[\frac{z_2(z_2+z_3)}{z_3}\right] \\
&= C\mathcal{Q}\left[-\frac{1}{z_3}\right]\mathcal{O}
\end{aligned} \tag{5}$$

In lines 2-4 of Eq. (5), $1/z_1$ is substituted using Eq. (3), exponential terms are collected, and a relationship (Table 5.1, pg. 118 (*37*)) between operators $\mathcal{R}$ [a] $\mathcal{Q}$ [c] is used to expand terms. Assuming that the illumination is uniform, the operators $\mathcal{V}$ [$(z_2+z_3)/z_3$] $\mathcal{R}$ [$z_2(z_2+z_3)/z_3$] are constants collected into C. Finally, the ordering of $\mathcal{Q}$ [$-1/z_3$] and $\mathcal{O}$ is commutative giving the final expression in Eq. (23).

The field at the aperture plane of the imaging lens is given by

$$\begin{aligned}\mathcal{S}_2\mathcal{O}\mathcal{S}_1 &= \mathcal{R}[z_3]\cdot C\mathcal{Q}\left[-\frac{1}{z_3}\right]\mathcal{O} \\ &= C\mathcal{Q}\left[\frac{1}{z_3}\right]\mathcal{V}\frac{1}{\lambda z_3}\mathcal{F}\mathcal{Q}\left[\frac{1}{z_3}\right]\mathcal{Q}\left[-\frac{1}{z_3}\right]\mathcal{O} \\ &= C\mathcal{Q}\left[\frac{1}{z_3}\right]\mathcal{V}\left[\frac{1}{\lambda z_3}\right]\mathcal{F}\mathcal{O}\end{aligned} \tag{6}$$

A relation (Eq. (5-51), pg. 117 (*37*)) between the operators is used to expand $\mathcal{R}[z_3]$, and two quadratic phase terms cancel, resulting in the final expression in Eq. (6).

At this point, we have a field at the aperture plane of the imaging lens that is a scaled Fourier transform of the object's field with an additional quadratic phase term. This coincides with the Fraunhofer diffraction approximation used to begin the analysis of the forward model presented in Section II. The rest of the analysis proceeds as described in the paper.

D. Discretization Using USAF Resolution Chart

Diffraction blur is inversely proportional to the diameter of the aperture; a linear increase in aperture diameter should result in a linear increase in resolution. However, the results in Fig. 5(D) seem to suggest a sub-linear increase in spatial resolution with respect to synthetic aperture size. The source of the discrepancy arises from the discrete resolutions measured by the USAF resolution target.

In the USAF target, the number of line pairs per millimeter increase logarithmically between neighboring elements–each element is $2^{1/6}$ times closer together than the preceding element. As a result of discretization and the logarithmic spacing, smaller gains in resolution are oversampled compared to large resolution improvements. For example, there are 6 measurements between a 1× and 2× increase in resolution but there are also only 6 measurements between an 8× and 16× gain in resolution. To illustrate the effect this has resolution measurements, discrete bar resolutions are plotted along with the previously recorded resolution measurements in fig. S4. The predicted resolution improvement (dashed orange line) is linear with diameter size; however, the discretized resolutions (blue dotted line) can only approximate the prediction in a stair-step manner. The measured resolutions for each synthetic aperture size are shown as purple 'x's. Due to the logarithmic spacing, the run of each stair increases between measurements, disproportionately affecting larger resolution gains. In our experiment, a synthetic aperture of 15.1 mm is created, a which should result in a 6.04× improvement in resolution. Due to the spacing of the resolution bars, the reported resolution is only 5.65× better than the resolution measured without using SAVI.

Showing a reconstruction of the USAF target has become *de rigueur* in Fourier ptychography papers, and offers a familiar and intuitive object for readers to understand. We have elected to use the USAF

resolution target to offer a direct comparison with the work of Tippie *et al.* (*11*). Horstmeyer *et al.* (*64*) suggest using a Siemens star as a more appropriate resolution target for reporting performance gains in coherent microscopy. Hopefully with the work in (*64*) the field will make the transition to using the more robust Siemens star.

E. Algorithm Convergence

Convergence of the proposed algorithm using the full dataset with denoising regularizer is shown in fig. S5. The images presented in fig. S5 are subsets of the USAF target shown in Fig. 5, where each image has been cropped to the first zoomed in feature (middle column) of Fig. 5(A). The initial estimate of $\Psi(\mathbf{u})$ is taken to be the average of the captured intensity images, fig. S5(B), that is upsampled and brought into the Fourier domain. After only a handful of iterations (fig. S5(C)), phase retrieval quickly returns an estimate of $\psi(\mathbf{x})$ that resolves features well beyond the diffraction limit of any single captured image fig. S5(A). Successive iterations of the image recovery algorithm further refine spatial resolution and reduces intensity variation due to speckle, fig. S5(D–F).

F. Recovering Phase Estimates

At the heart of SAVI is a phase retrieval algorithm to recover a high-resolution estimate of the field emanating from the object. When surface height profile of a diffusely scattering object is randomly distributed which introduces a random phase profile in the reflected wavefront. When recovering the high-resolution estimate of ψ, an estimate of the phase is also obtained. An example of the recovered phase for the $2 bill is shown in fig. S6. As expected, the recovered phase is randomly distributed between $[-\pi, \pi]$. If the spatial resolution could be increased to half of the wavelength of the illumination source the recovered phase map would directly correspond to the surface profile of the object in question. When the spatial resolution is not on the order of one wavelength, the recovered phase map will appear to be a random distribution. As our goal is to recover a high-resolution intensity image of the scene, the randomness in the phase map does not pose a problem.

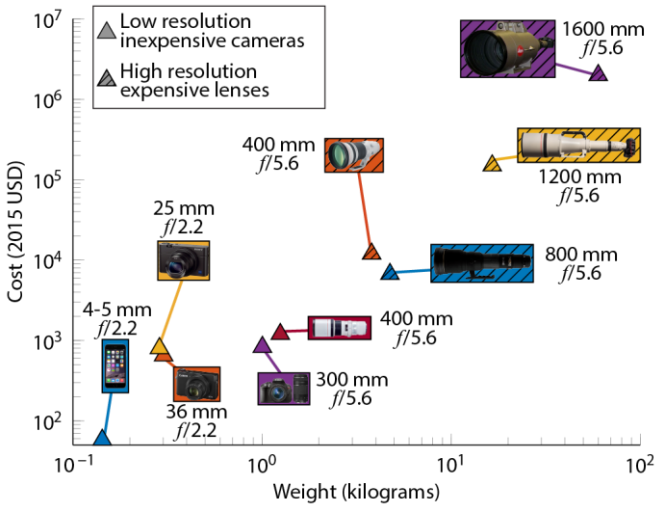

fig. S1. Cost and weight increase rapidly when improving lens resolution. Optically increasing spatial resolution requires using a lens of greater focal length. Simply using a larger lens to improve resolution may be prohibitively expensive. To keep diffraction blur in check, the ratio between the focal length and aperture diameter must be maintained, which demands drastic increase in size of the lens. Consequently, the weight and cost of the optics increase exponentially. The cost and weight of various commercial camera lenses ranging from cell-phone cameras to exotic super-telephoto lenses are plotted on a log-log scale with cost normalized to 2015 US dollars. The figure has been adapted from (*32*).

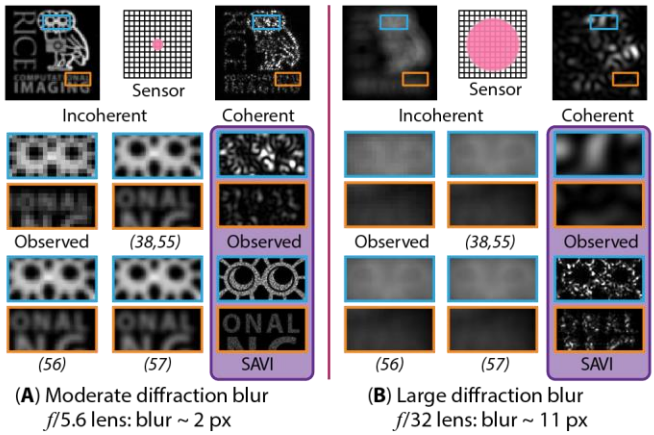

fig. S2. Comparison with incoherent superresolution methods for diffuse surfaces. Three common super-resolution methods are tested for (**A**) moderate diffraction blur and (**B**) large diffraction blur. The pink circle on the sensor denotes the radius of the diffraction spot size (the sensor size is constant). Papoulis-Gerchberg super-resolution (*38*, *55*), robust super-resolution (*56*), and normalized convolution (*57*) techniques are implemented using code from (*58*). Performance of incoherent super-resolution methods is unaffected by diffuse surfaces, as with optically smooth objects, performance gains are moderate for small diffraction blur and non-existent for large diffraction blur. Coherent illumination required for SAVI produces speckle in the observed measurements, which further degrades imaging performance. Nevertheless, recovering a larger synthetic aperture offers significant improvements in resolution even in the presence of large diffraction blur.

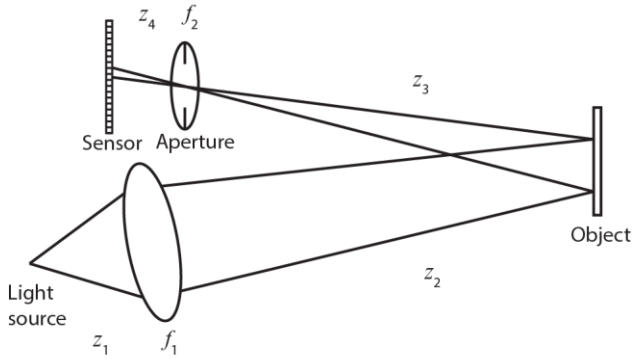

fig. S3. A simplified depiction of the imaging geometry.

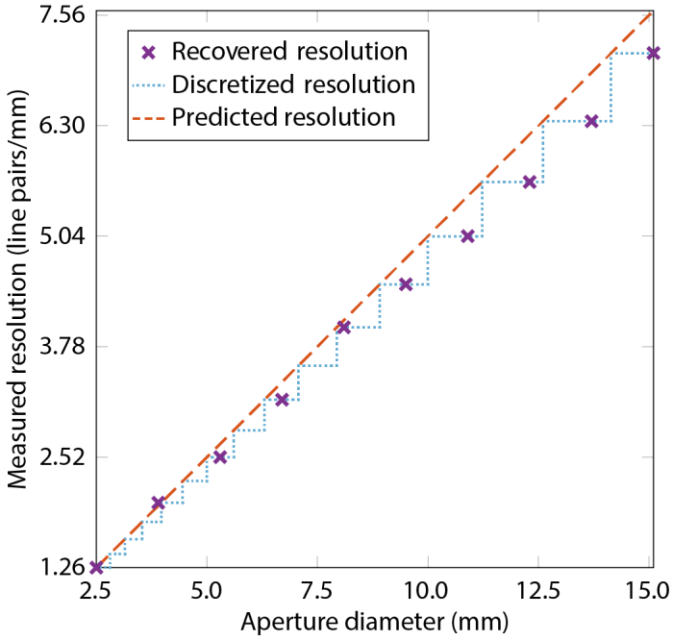

fig. S4. Discretization in the USAF resolution chart. As discussed in Fig. 5(**D**), resolution should improve linearly with SAS. However, the measured values deviate from the predicted curve due to the discretization of the USAF resolution target. Each element in the target is $2^{1/6}$ times smaller/larger than its neighboring elements. The discrete exponential distribution of spacings disproportionally affects larger SAS values. Measured resolution for each increase in SAS is shown as purple x's, the theoretical resolution improvement is shown as an orange dashed line, while the actual resolution values provided by the USAF target are shown as a blue dotted line.

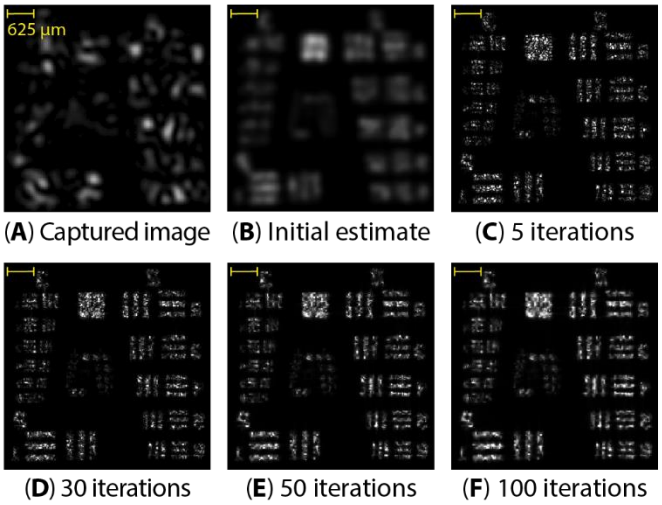

fig. S5. Convergence of proposed phase retrieval algorithm. Progress of the FP recovery algorithm is shown for the USAF target (full dataset with denoising). The images presented are insets of the scene corresponding to the first zoom-in region (middle column) of Fig. 5(**A**). Snapshots of the recovery are shown for (**A**) a captured intensity measurement, (**B**) the initialization that is an average of all captured images, (**C**-**F**) 5, 30, 50, and 100 iterations. The FP recovery algorithm rapidly returns a reasonable high-resolution image (C) before refining errors to reach the smallest resolvable features (D) and reducing the influence of speckle noise (E-F). The amount of speckle present in the estimate decreases while resolvability is maintained. The yellow scale bars on each of the reconstructions correspond to 625 µm.

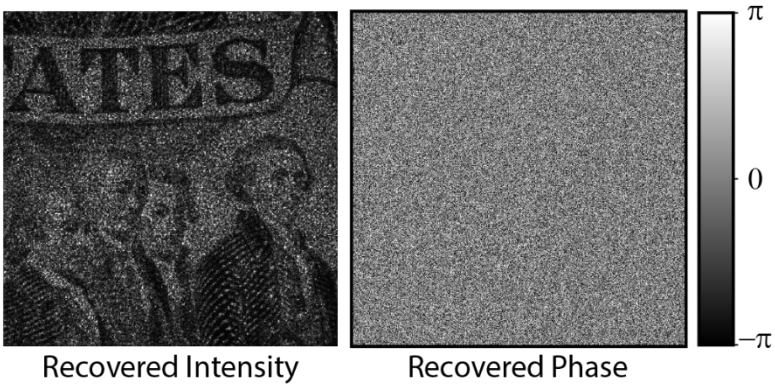

fig. S6. Example of recovered phase map. Optically rough objects exhibit a random surface height profile which leads to a random phase distribution. When recovering a high-resolution image (left) an estimate of the phase (right) is also obtained. As expected, the recovered phase map is seemingly random and difficult to interpret.